Article

Strain Engineered Electrically Pumped SiGeSn Microring Lasers on Si

Bahareh Marzban,[△] Lukas Seidel,[△] Teren Liu,[△] Kui Wu, Vivien Kiyek, Marvin Hartwig Zoellner, Zoran Ikonic, Joerg Schulze, Detlev Grützmacher, Giovanni Capellini, Michael Oehme, Jeremy Witzens,* and Dan Buca*

Read Online

ACCESS | Metrics & More | Article Recommendations

ABSTRACT: SiGeSn holds great promise for enabling fully group-IV integrated photonics operating at wavelengths extending in the mid-infrared range. Here, we demonstrate an electrically pumped GeSn microring laser based on SiGeSn/GeSn hetero-structures. The ring shape allows for enhanced strain relaxation, leading to enhanced optical properties, and better guiding of the carriers into the optically active region. We have engineered a partial undercut of the ring to further promote strain relaxation while maintaining adequate heat sinking. Lasing is measured up to 90 K, with a 75 K T_0. Scaling of the threshold current density as the inverse of the outer circumference is linked to optical losses at the etched surface, limiting device performance. Modeling is consistent with experiments across the range of explored inner and outer radii. These results will guide additional device optimization, aiming at improving electrical injection and using stressors to increase the bandgap directness of the active material.
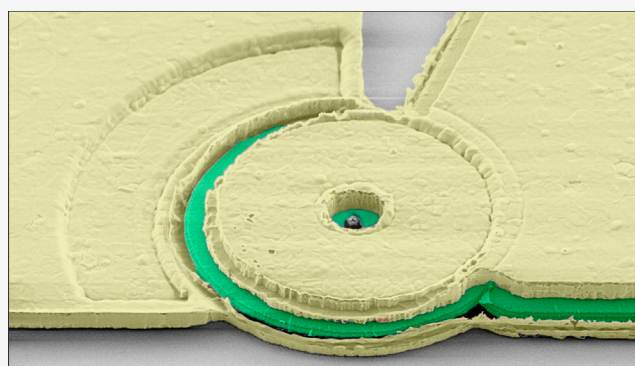
INTRODUCTION

Silicon (Si)-germanium (Ge)-tin (Sn) is a novel group-IV material system with great promise for monolithically integrating Si electronics and photonics. Large bandgap tunability via alloy composition allows fabrication of devices covering a broad range of the infrared spectrum, from 1.6 to 5 μm, while being potentially compatible with manufacturing within the cost-effective complementary metal-oxide-semi-conductor (CMOS) technology. Sensing, free-space communications, or very short reach interconnects are fast-growing applications that could greatly benefit from the extension of Si-photonics into the mid-infrared or the availability of CMOS-compatible light sources.[1] As an example, distributed monitoring of green-house gases at industrial or agricultural facilities requires cost-effective sensors, motivating monolithic integration[2] and operation at long wavelengths at which strong molecular absorption lines provide an effective means for quantitative measurements. In communications, resource disaggregation in server racks,[3] distributed machine-learning,[4] and signal distribution in phased-array antenna systems[5] create a need for highly integrated short-reach interconnects while being compatible with nonconventional wavelengths. Further-more, emerging photonically enabled neuromorphic hardware-accelerators,[6] as well as the data bottleneck in cryostats used in spin-qubit and superconductor-based quantum-computing

systems,[7,8] create further needs for unconventional short-reach optical interconnects that are either fully integrated at the chip-scale or work at cryogenic temperatures.

While progress has been made in light detection,[9,10] the realization of electrically pumped group-IV lasers fulfilling all the requirements for these applications remains an essential goal. Remarkable progress has been made with heterogeneous and monolithic integration of III−V materials on the Si platform.[11] However, SiGeSn provides the essential advantage of being fully composed of group-IV elements. Here too, much progress has been made since the first demonstration of an optically pumped GeSn-on-Si laser.[12] The (optically pumped) lasing temperature has been increased to room temperature (305 K).[13−15] Quantum-well lasers[16] as well as continuous-wave operation[17] have been demonstrated. Recently, electrical pumping has been reported, but restricted to very long Fabry−Perot cavities and thick epitaxial stacks in which light is vertically confined.[18,19]
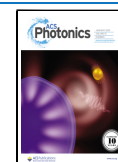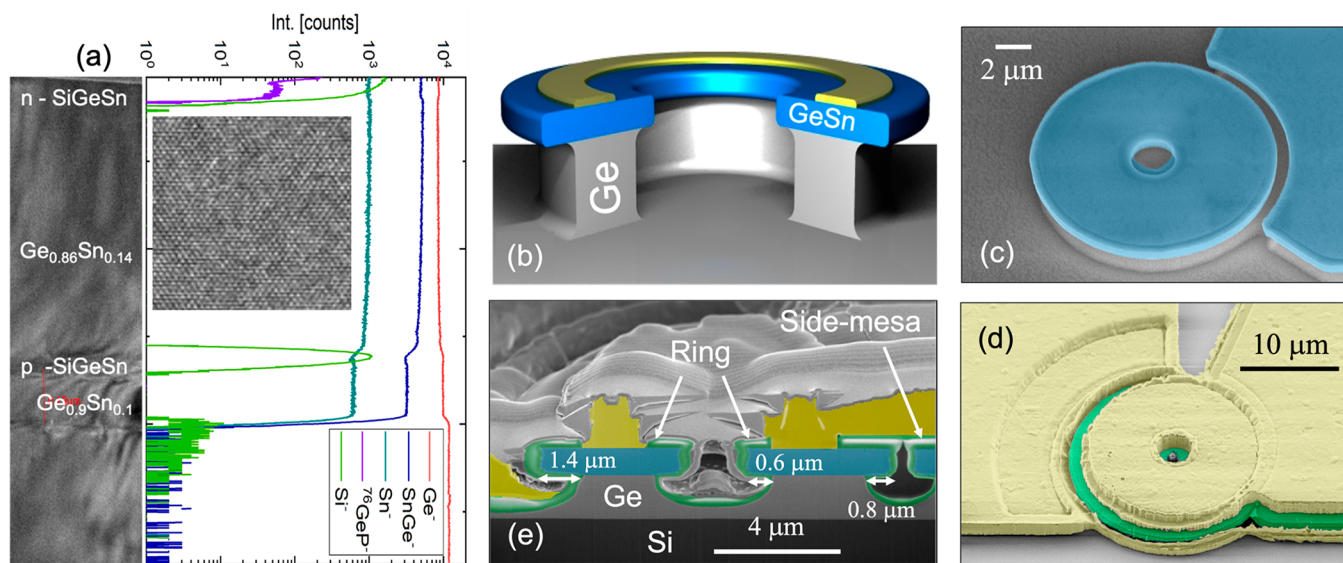
Figure 1. Laser material and processing. (a) Cross-section of the as-grown SiGeSn/GeSn heterostructure overlapped with the SIMS spectra. The HR-TEM inset is taken in the middle of the $Ge_{0.86}Sn_{0.14}$ active layer and indicates the high crystalline quality of the gain medium. (b) Schematic 3D view of the underetched microdisk laser. (c−e) SEM micrographs of the MRLs in false coloring. (c) Top view of a partially processed device in which the epitaxial stack has been etched and the undercut applied. The side mesa later used for topside contacting can be seen on the right. (d) Fully processed device imaged after metallization. (e) Cross-section of the microring with 1.13 μm inner and 5.5 μm outer hole radius. The rightmost mesa corresponds again to the side mesa for top-side contacting. Color coding: blue, GeSn/SiGeSn stack; golden, Al contacts; green, SiO_2 passivation and cladding. The topmost material in (e) is a conductive layer applied prior to the FIB cut to prevent charging and is not part of the device.

Based on learnings from optically pumped microdisk lasers, electrically pumped microring lasers (MRLs) have been designed. Undercut microdisk lasers consist in a small active material-stack supported by a pedestal etched into the underlying Ge virtual-substrate (VS).[16,20] This way, residual compressive strain built in during the epitaxial growth is relaxed, increasing the energy separation between the L- and Γ-valleys, the material "directness" $\Delta E_{L\Gamma}$. This increases the material gain and extends the temperature range in which lasing is obtained. However, thin pedestals, while optimum for elastic strain relaxation, compromise heat sinking that is particularly critical for electrically pumped membrane lasers.[21] Wide pedestals, on the other hand, constrain elastic strain relaxation to occur primarily along the radial direction along which the disk freely expands. Higher residual compressive strain in the azimuthal direction then favors gain for the azimuthal polarization and is detrimental to the amplification of whispery gallery modes (WGM), that are orthogonally polarized. To address this, we propose a ring shaped and partially undercut laser design. In addition to facilitating bidirectional strain relaxation, it improves routing of carriers to the optically active region and reduces the volume that needs to be pumped. Electrically pumped lasing is measured up to 90 K with a threshold current-density as low as 25 kA/cm^2 at 5 K for the larger, 9 μm outer radius rings, consistent with simulations.[22]

◼ MATERIAL AND DEVICE DESIGN

The SiGeSn/GeSn/SiGeSn double heterostructure (DHS) is grown in an industrial reduced-pressure chemical-vapor-deposition reactor (RPCVD) on 200 mm Si(100) wafers buffered with a 1.6 μm thick Ge-VS p-doped to 1×10^{18} cm^{-3}. Bottom-to-top, the heterostructure consists of (i) a 155 nm $Ge_{0.9}Sn_{0.10}$ buffer layer, (ii) a 20 nm $Si_{0.08}Ge_{0.84}Sn_{0.08}$ barrier

layer, (iii) a 760 nm $Ge_{0.86}Sn_{0.14}$ active layer, and (iv) an $Si_{0.05}Ge_{0.84}Sn_{0.11}$ barrier layer n-doped with phosphorus. The latter is composed of 60 nm doped to 2×10^{18} cm^{-3}, followed by 20 nm 5×10^{19} cm^{-3}, and facilitates the injection and transport of electrons into the active region with a reasonable series resistance. For holes, the device relies on defectivity driven p-doping of the lower layers.[22] Prior to undercut, the as-grown optically active material features −0.35% biaxial compressive heteroepitaxial strain determined by X-ray diffraction. Figure 1a shows a transmission electron micrograph (TEM) of the heterostructure together with its elemental distribution obtained by secondary ion mass spectrometry (SIMS). The relaxed $Ge_{0.9}Sn_{0.1}$ buffer provides a larger lattice constant that reduces the built-in strain in the following active layer, allowing a larger thickness growth.[16] The misfit networks at the GeSn buffer interfaces to the Ge-VS and SiGeSn barrier indicate lattice relaxation. The point and extended defects induced by the heteroepitaxy in the GeSn layer can be modeled as acceptor-like states[23] with a density of ∼5×10^{17} cm^{-3}.

A schematic of the MRL is shown in Figure 1b. The mesa is obtained by etching the SiGeSn/GeSn heterostructure down to the Ge-VS in an inductively coupled-plasma reactive-ion-etcher (ICPRIE) and is subsequently undercut by isotropically and selectively etching the Ge-VS in a plasma.[24,25] The underetch length of 1.4 μm is timed such that 200 nm Ge are left on the Si substrate to electrically connect the device to the bottom contact. Figure 1c shows a scanning electron micrograph (SEM) of a partially processed device in which the epitaxial stack has been etched and undercut. It reveals a side mesa for later topside contact metallization support. For passivation and to locally bridge the gap between the mesas, a 450 nm SiO_2 layer is deposited. Prior to metallization, windows have been opened on top of the ring as well as on

the bottom Ge film in the form of an annulus sector. Finally, 2 μm of aluminum (Al) is sputtered and structured with HBr, leading to the device structure shown in Figure 1d.

MRLs with different outer radii, R_o, and inner radii, R_i, between 0 and 1 μm were targeted. Cross-sectional micrographs (Figure 1e) reveal that the 1.4 μm undercut along the outer edge of the ring reduces to ~0.8 μm close to the adjacent mesa due to restricted gas flow. Simulation results indicate that the variability of the outer undercut does not result in significant optical losses compared to free carrier absorption (FCA) and scattering (mode overlap at the discontinuity >99% and substrate coupling losses <1 cm^{-1}). The etch process also leads to the undercut at the inner hole to be strongly radius-dependent (Table 1), which we shall see greatly impacts the device performance.

Table 1. Geometric Parameters of Fabricated Devices

device	A	B	C	D
outer radius (R_o)	5.5 μm	5.5 μm	5.5 μm	5.5 μm
inner radius (R_i)	0	580 nm	825 nm	1.13 μm
outer undercut (w_{4o})	1.4 μm	1.4 μm	1.4 μm	1.4 μm
inner undercut (w_{4i})	NA	0	0.6 μm	0.6 μm
outer rim to electrode (w_1)	1.5 μm	1.5 μm	1.5 μm	1.5 μm
inner rim to electrode (w_2)	1.25 μm[a]	920 nm	925 nm	870 nm

[a]Defined for device A as distance from center.

A number of considerations have entered the design. WGMs provide straightforward separation between the top electrode and the optical field without requiring vertical mode confinement in a thick heterostructure. However, the spacing between the top electrode and the outer ring periphery (w_1) results in a trade-off between optical losses and carrier injection efficiency and was chosen as 1.5 μm. Simulations indicate negligible absorption losses (≪1 cm^{-1}) that would reach ~1 cm^{-1} if w_1 were to be reduced to 1 μm. However, these do not consider possible alloying and spiking at the Al contact, so that actual losses might be higher and the geometry was conservatively chosen. The presence of the bottom electrode does not impact simulated losses, due to the rapid decay of the field in the SiO$_2$ and air cladding. The outer radius impacts both the scattering and the surface absorption losses at the etched interface.[26,27] Finally, the inner radius modifies the current flow and the anisotropy of the in-plane strain relaxation. Importantly, despite of the ring geometry, the cavities behave optically like disks, since the inner surface is too far to influence the optical mode.

The inset in Figure 2a shows an exaggerated representation of the deformation after undercut. Due to strain mismatch between underlying buffer and overlying active material, the structure bows downward at its periphery (24 nm for $R_i = 1$ μm, $R_o = 5.5$ μm), while extending radially, which leads to the variation in strain seen along the vertical direction in Figure 2b. Figure 2b,c shows the corresponding strain profiles, obtained from mechanical modeling (COMSOL Multiphysics), along vertical and horizontal cuts (dotted yellow lines, Figure 2a) and takes this deformation into account. The vertical cut is taken close to the periphery, where the optical field of the transverse electric (TE) and transverse magnetic (TM) WGM ground modes are maximum. The horizontal cut is taken at the middle of the active material. The undercut reduces the

average in-plane compressive strain from −0.35% to −0.05%, increasing the gain material directness. The inner hole slightly reduces the difference between the radial ε_{rr} and azimuthal $\varepsilon_{\theta\theta}$ strain components, improving the gain for the TE WGMs by 11%, at equal free carrier concentration. The flat-band energy diagram, that is, before applying dopants in the simulations, is calculated via eight-band $k \cdot p$ theory along the vertical cut, assuming the strain at the center of each layer (Figure 2d). The undercut improves the directness from 40 to 70 meV, calculated using modified bowing parameters found to best fit experimental results.[28]

Figure 2e shows the net modal gain versus injection-current density, at 50 K, for devices with $R_o = 5.5$ μm, following previously made modeling assumptions.[22,28] Both a disk without inner hole and a ring with $R_i = 1$ μm, that correspond to devices A and D (see Table 1), are modeled. For the ring's inner hole, the actual undercut length obtained from the cross-sectional TEM has been considered. It can be seen that the gain of the TE$_0$ ground mode (blue) is higher than that of TM$_0$ (red). Furthermore, we clearly see the gain enhancement induced by the presence of the inner hole. Modeling shows that this is primarily due to a better guiding of the carriers toward the optically active region, at the ring's outer periphery, since central regions are now etched away or undercut. A larger undercut at the inner hole would increase this enhancement further. In this modeling, FCA, including intervalence-band absorption (IVBA), are taken into account. Surface-induced scattering and absorption losses are not included, but discussed later with the measurements. Assuming 450 cm^{-1} results in the best fit and a 62 kA/cm^2 (59 mA) threshold for the disk, larger than the 49 kA/cm^2 (45 mA) calculated for the ring. The gain material transparency threshold is calculated as 17 kA/cm^2.

The net gain for the ring's TE$_0$ mode versus photon energy for different injection-current densities is presented in Figure 2f. If we neglect carrier-induced bandgap narrowing, with the assumed 450 cm^{-1} scattering and surface absorption, we obtain a peak gain emission energy of 467 meV.

■ MEASUREMENT RESULTS

The MRLs were measured in a cryostat applying 100 ns current pulses with a 20 μs repetition time using a spectrometer with a 2 cm^{-1} resolution bandwidth. We first report measurements for a series of four lasers with a common 5.5 μm R_o, but varying R_i, with characteristics summarized in Table 1.

The lasing spectra of MRL D, with the largest inner radius, are presented in Figure 3. Linewidths are consistently ~1 nm, limited by the spectrometer resolution. The device lases up to a cryostat temperature of 90 K, beyond which the rapid increase in threshold prevented us from maintaining laser action without damaging the metallic contacts. Up to 60 K, the laser emission is monomode at an energy of 462 meV ($\lambda = 2681$ nm). At higher temperatures, it switches to 454 meV ($\lambda = 2730$ nm) for currents close to threshold, which corresponds to one free spectral range (FSR) calculated as 50 nm given the TE$_0$ group index of 4.22 predicted from a finite-elements mode solver (Lumerical). It results from thermally induced bandgap narrowing. Unfortunately, the TM$_0$ FSR is very close (49 nm), so that this observation is insufficient to confirm the TE polarization expected from modeling. At higher currents, the device lases in both modes as a consequence of band filling.

The current-in light-out (LI) characteristic of the laser at 5 K is shown on a log−log scale in the inset of Figure 3a and
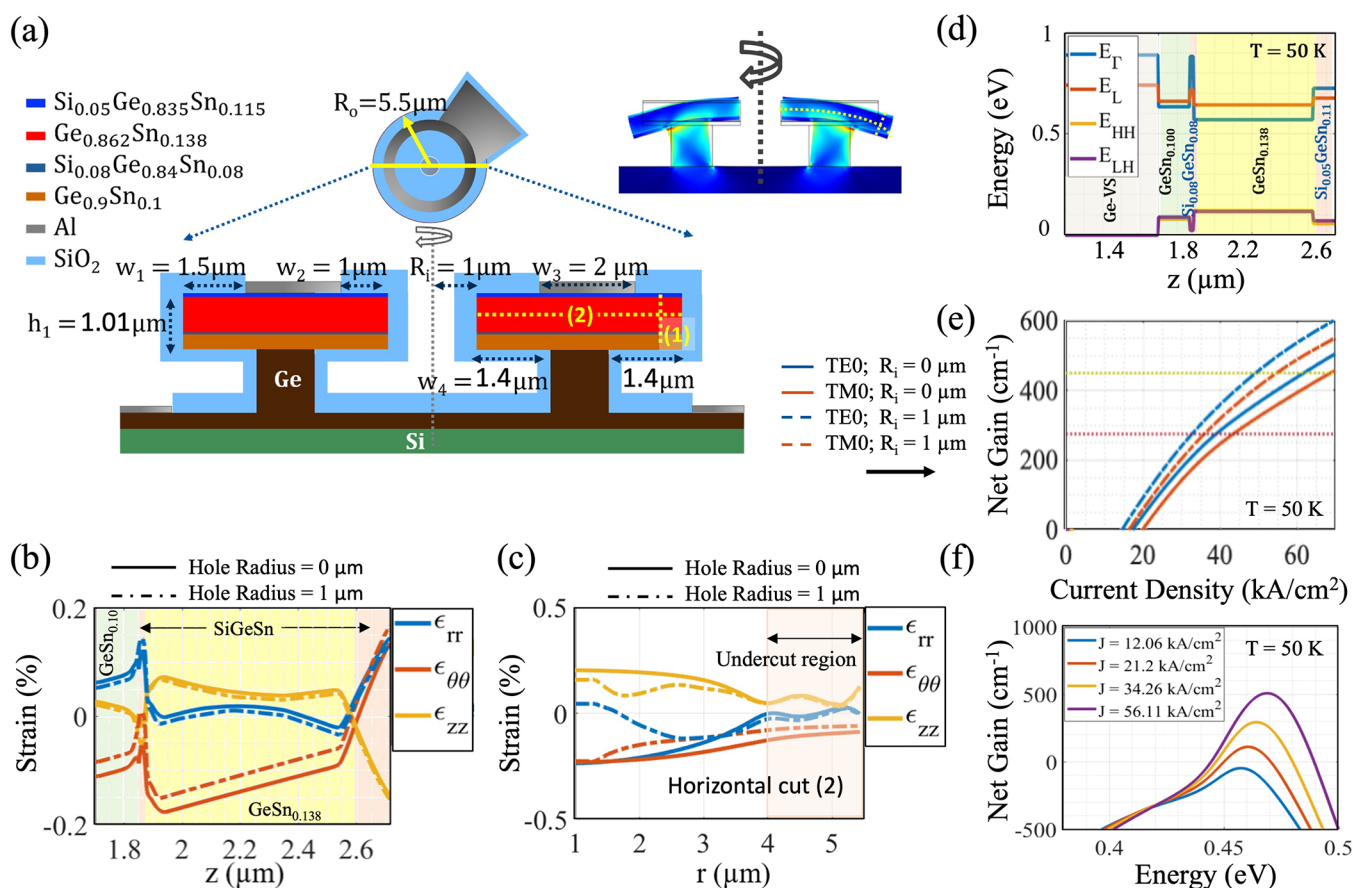
Figure 2. Laser concept and modeling results. (a) Cross-sectional diagram of an MRL with labeled dimensions. The inset directly on top shows a top view in which the position of the cross-section is marked in yellow. The inset to the right shows the result of mechanical modeling, in which displacements are exaggerated in order to make them visible. (b) and (c) show the strain along the vertical and radial directions, respectively along the vertical and horizontal cuts shown as dotted yellow lines and labeled as (1) and (2) in (a) (they are also indicated in the deformed structure, that actually enters further modeling). The solid lines show the modeling results when the inner hole is not present (disk geometry), while the dot-dashed lines correspond to a microring laser with a 1-μm-radius inner hole applied to the stack prior to undercut. (d) Band edges along the vertical cutline after mechanical relaxation (HH: heavy holes, LH: light holes). Numerical values are taken at the center of each layer. Calculated net modal gain at a temperature of 50 K as a function of (e) the injection current density (TE$_0$ and TM$_0$, with and without inner hole) and (f) the photon energy for the TE$_0$ mode of the undercut microring laser at different currents. The net modal gain shown in (e) and (f) includes the effect of FCA and IVBA, but does not include scattering and surface absorption losses. The calculations in (f) do not take carrier-induced bandgap narrowing into account. Both are discussed in the text. The undercut at the inner edge of the ring is also assumed to be reduced to 0.7 μm to match the process bias observed in the fabricated devices. Threshold current densities are normalized relative to the area of the SiGeSn layer. The dotted horizontal lines in (e) correspond to surface loss assumptions of 450 (yellow) and 275 cm^{-1} (purple) discussed in the text.

features the characteristic S-shape. The LI characteristics up to 90 K are shown in Figure 4a, while Figure 4b summarizes the slope efficiency and threshold current-density versus temperature. Between 5 and 80 K, the slope efficiency drops from 4.8 to 0.2 a.u./mA, while the threshold increases from 38.0 to 102.3 kA/cm^2. Temperature dependences closely follow expected exponential trends, so that the characteristic T_0 (threshold) and T_1 (slope efficiency) can be extracted as 74.5 and 27 K, respectively.

Calibration of the spectrometer data with a surface emitting light emitting diode (LED) suggests that the peak power collected from laser A at an 80 mA injection current (189 a.u.) is 217 μW. Given the 36 mA threshold of the device, this corresponds to a differential external quantum efficiency (EQE) of 1%. This number is higher than the 0.3% EQE previously reported for relatively long (800 μm) edge emitting GeSn lasers,[18] whose quantum efficiency may have been limited by internal absorption losses resulting from the high FCA in this material system.[28] Moreover, given that the

measured MRL emission is not directional but scattered light with a nonlambertian profile, the collection efficiency of the spectrometer is reduced compared to the LED reference measurement. Taking this as well as partial reflection from the Si substrate into account (the device emits both upward and downward), the actual EQE is expected to be higher by about a factor 3. In addition to modal absorption losses, scattering of light into dissipated higher-order modes constitutes another pathway competing with outcoupling of the light. Controlled outcoupling into a waveguide thus constitutes an essential future development.[29]

A summary of the laser thresholds at 50 K for lasers A–D, whose inner radius varies between 0 and 1.13 μm, is shown in Figure 4c. Except for the inner undercut length, all other parameters remain identical within the fabrication process variability. The lasing threshold improves by 18% at the largest inner radius. Since the light hole (LH) to heavy hole (HH) band-splitting causing the gain anisotropy is already relatively small in device A (9 meV), this improvement originates
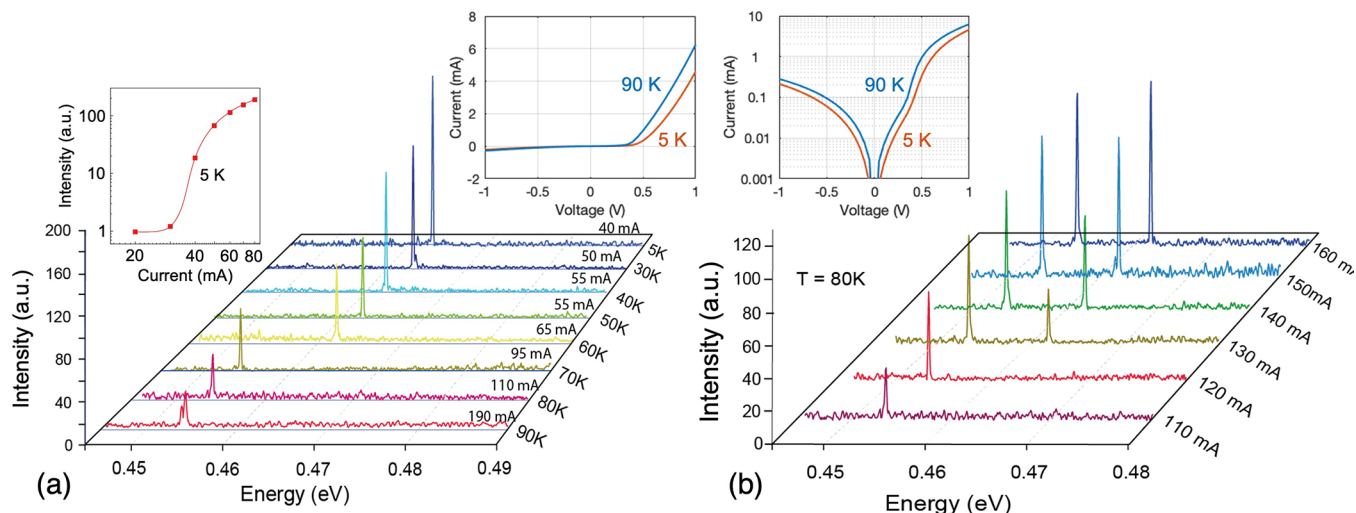
Figure 3. Emission spectra of selected devices. Lasing spectra of the MRL with $R_i = 1.13\ \mu m$ and $R_o = 5.5\ \mu m$ at (a) different temperatures and (b) different injection currents at 80 K. A mode hop by one FSR toward higher energies is visible at lower temperatures and higher pump currents, respectively attributed to the thermal dependence of the bandgap energy and band filling increasing the gain at higher photon energy. The inset to the left shows the LI curve at 5 K on a log−log scale and features the characteristic S-shape of lasers. The two insets to the right show IV curves taken under DC conditions at 5 and 90 K on a linear and semilog scale.
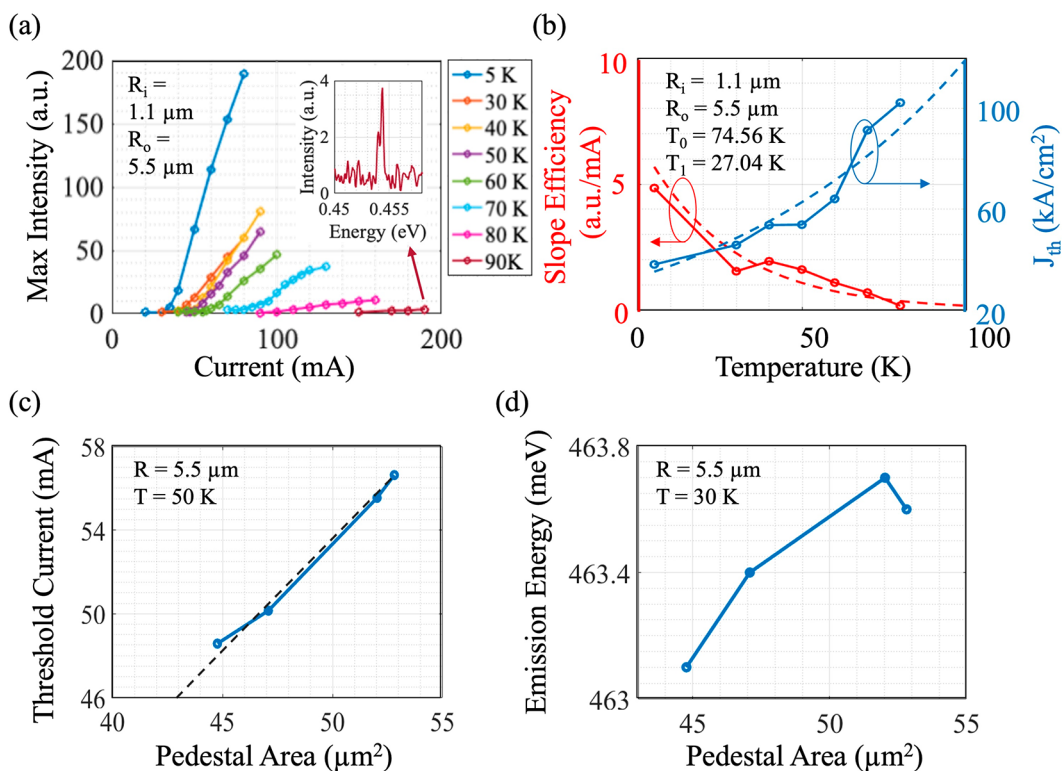
Figure 4. Summary of characteristics of lasers A−D, with fixed outer radius (5.5 μm) and varied inner radius. (a) LI curves of the MRL with $R_i = 1.13\ \mu m$ between 5 and 90 K. The inset shows the spectrum at 90 K and 190 mA. (b) Summary of the extracted threshold current density (J_{th}) and slope efficiency for this laser, as a function of temperature. The dashed lines show the exponential fits used to extract T_0 and T_1. The slope efficiency is obtained from the derivative of the LI curves. (c) Threshold current at a fixed 50 K temperature, for different inner hole radii. It is plotted against the pedestal area, which reveals a close to linear dependency on the latter (linear fit with zero intercept: dashed curve). (d) Emission energy, at a fixed 30 K temperature, for different inner hole radii, also plotted against pedestal area, at a fixed 60 mA injection current.

primarily from better current guiding, as seen in simulations. Plotting the threshold current versus pedestal area reveals a close to linear dependence indicating that the current mainly flows through this region (the top electrode area scales with the pedestal and overlays it).

The emission energies of the four lasers, shown at 30 K and 60 mA in Figure 4d, decrease as the inner radius is increased and the underlying pedestal width decreased, consistent with expected material strain relaxation. These shifts, much below the FSR, follow the resonance position and not the gain spectrum, consequently revealing the induced refractive index

change. Taking the strain dependence in Ge for a rough estimation,[30] the observed 3.5 nm wavelength shift corresponds to about 0.06% in additional strain relaxation, in the bulk part of the mechanical simulations (0.03% additional strain relaxation in the azimuthal direction).[31]

Up to 70 K, the four lasers feature a T_0 of ~74 K. However, the diodes differ markedly at higher temperatures. Above 70 K, the thresholds increase much faster, suggesting that the conduction-band L-valley starts being populated, the usual reason for the threshold runoff in GeSn alloys.[28] While the threshold of the disk already significantly jumps up to 130 mA at 80 K, device D stays close to the T_0-trend at 80 K and jumps up to 170 mA 10 K later, even though it has reduced heat sinking. This confirms the improved directness of the gain material from additional elastic relaxation via inner hole underetch.

Fitting the experimental thresholds, excellent consistency is obtained with modeling by assuming 450 cm^{-1} surface absorption and scattering losses. At 50 K, the threshold is modeled as 59 mA and measured as 57 mA for device A, and modeled as 45 mA and measured as 48 mA for device D. The modeled peak gain energy at 467 meV is very close to the experimentally observed 463 meV emission, although a larger difference would have been expected given that bandgap renormalization has not been modeled. The next series of experiments sheds some more light onto the surface absorption losses:

We have measured lasers at 5 K with a fixed nominal inner radius $R_i = 1$ μm, as for device D, and various outer radii, R_o, between 5.5 and 9 μm. The thresholds, shown in Figure 5,
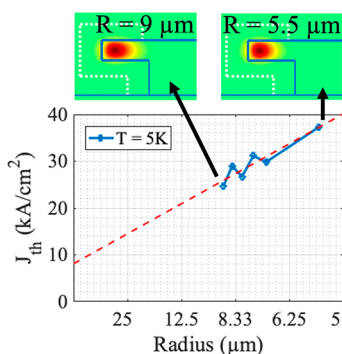
Figure 5. Lasing threshold densities for a series of lasers with fixed inner radius (~1 μm) as a function of the inverse outer radius at 5 K. The dependency on the outer radius follows a $1/R_o$ trend (fit shown as dashed curve). The threshold current densities are normalized relative to the area of the SiGeSn layer. The insets show the simulated WGMs for the smallest and largest outer radius device. The y-axis intercept suggests a transparency threshold of 8 kA/cm^2 at 5 K.

scale with the inverse of R_o. This trend has also been observed in III−V microdisk lasers and attributed to carrier recombination at the etched interface[32] or to optical scattering and surface absorption.[27] The relative weight of surface recombination in the overall carrier lifetime scales as the ratio of the circumference to the surface and thus as $1/R$.[32] However, following the model from Zhukov et al.[32] and assuming typical ~100 ps bulk carrier lifetimes for this gain material,[28] one needs to assume a surface recombination velocity of ~10^6 cm/s, which appears nonphysical. Furthermore, the data shown in Figure 4c suggests that recombination is not dominated by surface effects at the etched boundaries, since

threshold currents scale with the pedestal area. Consequently, the observed trend is attributed to surface induced optical absorption or scattering losses, which also scale with $1/R$ in microdisks as a consequence of the mode profile becoming larger with increasing disk radius (insets in Figure 5) and the overlap with the outer surface thus reducing.[26] The absorption losses can be indirectly caused by surface recombination depleting free carriers at the outer periphery.[27] While the widening mode profile also increases the overlap with the top electrode, corresponding losses remain negligible with the 1.5 μm w_1 (0.07 cm^{-1} for $R_o = 9$ μm).

At 50 K, the radius dependency is weaker and the experimental threshold current-density only drops by 20%, from 52 to 42 kA/cm^2, as opposed to the 40% drop seen at 5 K. This can be explained by the increased transparency threshold at higher temperatures leading to injection current and gain scaling increasingly differently from each other. The experimentally observed scaling is consistent with the modeled gain. Assuming optical losses to scale with $1/R$, we expect them to reduce to 275 cm^{-1} at $R_o = 9$ μm. The relevant gain curve is that of the disk (solid curves in Figure 2e), as at $R_o = 9$ μm the much smaller inner hole is not sufficient to make a significant difference. The predicted threshold current-density is then 39 kA/cm^2, very close to the experimental 42 kA/cm^2.

◼ DISCUSSION

As discussed, currently, the maximum lasing temperature is limited by the highest current that can be injected without damage. This maximum laser temperature is much below the 270 K lasing obtained by optical pumping of a 9 μm Ge$_{0.86}$Sn$_{0.14}$ microdisk laser grown using the same epitaxial procedure and RPCVD reactor.[15] Consequently, future work should focus on improving metal contacting, as well as the doping profiles to reduce unnecessary joule heating resulting from carrier transport. The current−voltage characteristics of the lasers with 5.5 μm outer radius reveal a ~120 Ω series resistance that can be significantly improved via in situ doping. From the design point of view, larger outer radii should allow reduction of the optical losses, but to fully leverage this the inner radius should also be increased accordingly. Furthermore, strain engineering[33] by silicon nitride stressors to induce tensile strain in the active GeSn region, that already enabled room temperature lasing under optical pumping,[15] provides a further path toward progress in the electrically pumped lasing temperature.

◼ CONCLUSIONS

We have experimentally fabricated and characterized electrically pumped SiGeSn/GeSn double heterostructure microring lasers that lase up to 90 K. Partial undercut allows strain relaxation while maintaining adequate heat sinking via the underlying Ge-VS. Lasers with different inner and outer radii have been characterized, revealing useful trends that are consistent with modeling with a cohesive set of assumptions. Increasing the inner radius improves strain relaxation and guiding of the carriers, respectively increasing the maximum lasing temperature and reducing the lasing threshold. Increasing the outer radius reduces the threshold current-density significantly, pointing at optical losses at the etched interface to play a significant role. Further improvements are expected by increasing both the inner and outer radius of the

structures, by applying stressor layers, and by improving the contact module.

■ AUTHOR INFORMATION

Corresponding Authors

Jeremy Witzens − *Institute of Integrated Photonics, RWTH Aachen University and JARA-Fundamentals of Future Information Technologies, 52074 Aachen, Germany;* ⬤ orcid.org/0000-0002-2896-7243; Email: jwitzens@iph.rwth-aachen.de

Dan Buca − *Peter Grünberg Institute 9, Forschungszentrum Jülich and JARA-Fundamentals of Future Information Technologies, 52428 Jülich, Germany;* Email: d.m.buca@fz-juelich.de

Authors

Bahareh Marzban − *Institute of Integrated Photonics, RWTH Aachen University and JARA-Fundamentals of Future Information Technologies, 52074 Aachen, Germany*

Lukas Seidel − *Institut für Halbleitertechnik, University of Stuttgart, 70569 Stuttgart, Germany*

Teren Liu − *Peter Grünberg Institute 9, Forschungszentrum Jülich and JARA-Fundamentals of Future Information Technologies, 52428 Jülich, Germany*

Kui Wu − *Institute of Integrated Photonics, RWTH Aachen University and JARA-Fundamentals of Future Information Technologies, 52074 Aachen, Germany*

Vivien Kiyek − *Peter Grünberg Institute 9, Forschungszentrum Jülich and JARA-Fundamentals of Future Information Technologies, 52428 Jülich, Germany;* Present Address: Institute of Energy and Climate Research − Materials Synthesis and Processing (IEK-1), Forschungszentrum Jülich, 52428 Jülich, Germany; Chair of Materials Synthesis for Energy Technologies, Institute of Mineral Engineering, RWTH Aachen University, 52072 Aachen, Germany

Marvin Hartwig Zoellner − *IHP-Leibniz Institut für innovative Mikroelektronik, 15236 Frankfurt (Oder), Germany;* ⬤ orcid.org/0000-0001-7204-1096

Zoran Ikonic − *School of Electronic and Electrical Engineering, University of Leeds, Leeds LS2 9JT, United Kingdom*

Joerg Schulze − *Institut für Halbleitertechnik, University of Stuttgart, 70569 Stuttgart, Germany;* Present Address: Lehrstuhl für Elektrische Bauelemente, University of Erlangen, 91058 Erlangen, Germany; Fraunhofer Institute for Integrated Systems and Device Technology (IISB), 911058 Erlangen, Germany

Detlev Grützmacher − *Peter Grünberg Institute 9, Forschungszentrum Jülich and JARA-Fundamentals of Future Information Technologies, 52428 Jülich, Germany*

Giovanni Capellini − *IHP-Leibniz Institut für innovative Mikroelektronik, 15236 Frankfurt (Oder), Germany; Department of Science, Roma Tre University, 00146 Rome, Italy*

Michael Oehme − *Institut für Halbleitertechnik, University of Stuttgart, 70569 Stuttgart, Germany*

Complete contact information is available at:
https://pubs.acs.org/10.1021/acsphotonics.2c01508

Author Contributions

△These authors contributed equally to this work.

Funding

Notes

The authors declare no competing financial interest.

■ ABBREVIATIONS

CMOS; complementary metal-oxide-semiconductor; DHS; double heterostructure; FCA; free carrier absorption; FIB; focused ion beam; FSR; free spectral range; Ge; germanium; ICP; inductively coupled plasma; IVBA; intervalence-band absorption; MRL; microring laser; PECVD; plasma-enhanced chemical vapor deposition; RIE; reactive ion etching; RPCVD; reduced pressure chemical vapor deposition; SEM; scanning electron microscope; Si; silicon; SIMS; secondary ions mass spectrometry; Sn; Tin; TE; transverse electric; TEM; transmission electron microscopy; TM; transverse magnetic; VS; virtual substrate; WGM; whispering gallery mode

■ REFERENCES

(1) Moutanabbir, O.; Assali, S.; Gong, X.; O'Reilly, E.; Broderick, C.; Marzban, B.; Witzens, J.; Du, W.; Yu, S.-Q.; Chelnokov, A.; Buca, D.; Nam, D. Monolithic Infrared Silicon Photonics: The Rise of (Si)GeSn Semiconductors. *Appl. Phys. Lett.* **2021**, *118*, 110502.

(2) Tombez, L.; Zhang, E. J.; Orcutt, J. S.; Kamlapurkar, S.; Green, W. M. J. Methane absorption spectroscopy on a silicon photonic chip. *Optica* **2017**, *4*, 1322−1325.

(3) Lin, R.; Cheng, Y.; De Andrade, M.; Wosinska, L.; Chen, J. Disaggregated Data Centers: Challenges and Trade-offs. *IEEE Com. Mag* **2020**, *58*, 20−26.

(4) Yan, S.; Zhu, Z.; Glick, M. S.; Wu, Z.; Bergman, K. Accelerating Distributed Machine Learning in Disaggregated Architectures with Flexible Interconnected Computing Resources. *Proc. Opt. Fib. Comm. Conf. (OFC)* **2022**, Th1G.2.

(5) Testa, F.; Wade, M. T.; Lostedt, M.; Cavaliere, F.; Romagnoli, M.; Stojanovic, V. Optical Interconnects for Future Advanced Antenna Systems: Architectures, Requirements and Technologies. *J. Lightwave Technol.* **2022**, *40*, 393−403.

(6) Ashtiani, F.; Geers, A. J.; Aflatouni, F. An on-chip photonic deep neural network for image classification. *Nature* **2022**, *606*, 501−506.

(7) Youssefi, A.; Shomroni, I.; Joshi, Y. J.; Bernier, N. R.; Lukashchuk, A.; Uhrich, P.; Qiu, L.; Kippenberg, T. J. A cryogenic electro-optic interconnect for superconducting devices. *Nat. Electron* **2021**, *4*, 326−332.

(8) Pintus, P.; Singh, A.; Xie, W.; Ranzani, L.; Gustafsson, M. V.; Tran, M. A.; Xiang, C.; Peters, J.; Bowers, J. E.; Soltani, M. Ultralow voltage, high-speed, and energy-efficient cryogenic electro-optic modulator. *Optica* **2022**, *9* (10), 1176−1182.

(9) Pham, T.; Du, W.; Tran, H.; Margetis, J.; Tolle, J.; Sun, G.; Soref, R. A.; Naseem, H. A.; Li, B.; Yu, S.-Q. Systematic study of Si-based GeSn photodiodes with 2.6 µm detector cutoff for short-wave infrared detection. *Opt. Exp.* **2016**, *24* (5), 4519−4531.

(10) Talamas Simola, E.; Kiyek, V.; Ballabio, A.; Schlykow, V.; Frigerio, J.; Zucchetti, C.; De Iacovo, A.; Colace, L.; Yamamoto, Y.; Capellini, G.; Grützmacher, D.; Buca, D.; Isella, G. CMOS-Compatible Bias-Tunable Dual-Band Detector Based on GeSn/Ge/Si Coupled Photodiodes. *ACS Photonics* **2021**, *8* (7), 2166−2173.

(11) Han, Y.; Park, H.; Bowers, J.; Lau, K. M. Recent advances in light sources on silicon. *Adv. Opt. Photon.* **2022**, *14*, 404−454.

(12) Wirths, S.; Geiger, R.; von den Driesch, N.; Mussler, G.; Stoica, T.; Mantl, S.; Ikonic, Z.; Luysberg, M.; Chiussi, S.; Hartmann, J. M.;

Sigg, H.; Faist, J.; Buca, D.; Grützmacher, D. Lasing in direct-bandgap GeSn alloy grown on Si. *Nat. Photon.* **2015**, *9*, 88−92.

(13) Chrétien, J.; Pauc, N.; Pilon, F. A.; Bertrand, M.; Thai, Q.-M.; Casiez, L.; Bernier, N.; Dansas, H.; Gergaud, P.; Delamadeleine, E.; Khazazka, R.; Sigg, H.; Faist, J.; Chelnokov, A.; Reboud, V.; Hartmann, J.-M.; Calvo, V. GeSn Lasers Covering a Wide Wavelength Range Thanks to Uniaxial Strain. *ACS Photonics* **2019**, *6*, 2462−2469.

(14) Zhou, Y.; Dou, W.; Du, W.; Ojo, S.; Tran, H.; Ghetmiri, S. A.; Liu, J.; Sun, G.; Soref, R.; Margetis, J.; Tolle, J.; Li, B.; Chen, Z.; Mortazavi, M.; Yu, S.-Q. Optically Pumped GeSn Lasers Operating at 270 K with Broad Waveguide Structures on Si. *ACS Photonics* **2019**, *6* (6), 1434−1441.

(15) Buca, D.; Bjelajac, A.; Spirito, D.; Concepción, O.; Gromovyi, M.; Sakat, E.; Lafosse, X.; Ferlazzo, L.; von den Driesch, N.; Ikonic, Z.; Grützmacher, D.; Capellini, G.; El Kurdi, M. Room Temperature Lasing in GeSn Microdisks Enabled by Strain Engineering. *Adv. Opt. Mater.* **2022**, *10*, 2201024.

(16) Stange, D.; von den Driesch, N.; Zabel, T.; Armand-Pilon, F.; Rainko, D.; Marzban, B.; Zaumseil, P.; Hartmann, J.-M.; Ikonic, Z.; Capellini, G.; Mantl, S.; Sigg, H.; Witzens, J.; Grützmacher, D.; Buca, D. GeSn/SiGeSn Heterostructure Multi Quantum Well Lasers. *ACS Photon.* **2018**, *5*, 4628−4636.

(17) Elbaz, A.; Buca, D.; von den Driesch, N.; Pantzas, K.; Patriarche, G.; Zerounian, N.; Herth, E.; Checoury, X.; Sauvage, S.; Sagnes, I.; Foti, A.; Ossikovski, R.; Hartmann, J.-M.; Boeuf, F.; Ikonic, Z.; Boucaud, P.; Grützmacher, D.; El Kurdi, M. Ultra-low-threshold continuous-wave and pulsed lasing in tensile-strained GeSn alloys. *Nat. Photon.* **2020**, *14*, 375−382.

(18) Zhou, Y.; Miao, Y.; Ojo, S.; Tran, H.; Abernathy, G.; Grant, J. M.; Amoah, S.; Salamo, G.; Du, W.; Liu, J.; Margetis, J.; Tolle, J.; Zhang, Y. H.; Sun, G.; Soref, R. A.; Li, B.; Yu, S.-Q. Electrically injected GeSn lasers on Si operating up to 100 K. *Optica* **2020**, *7*, 924−928.

(19) Zhou, Y.; Ojo, S.; Wu, C.-W.; Miao, Y.; Tran, H.; Grant, J. M.; Abernathy, G.; Amoah, S.; Bass, J.; Salamo, G.; Du, W.; Chang, G.-E.; Liu, J.; Margetis, J.; Tolle, J.; Zhang, Y.-H.; Sun, G.; Soref, R. A.; Li, B.; Yu, S.-Q. Electrically injected GeSn lasers with peak wavelength up to 2.7 μm. *Photon. Res.* **2022**, *10* (1), 222−229.

(20) Stange, D.; Wirths, S.; Geiger, R.; Schulte-Braucks, C.; Marzban, B.; von den Driesch, N.; Mussler, G.; Zabel, T.; Stoica, T.; Hartmann, J.-M.; Mantl, S.; Ikonic, Z.; Grützmacher, D.; Sigg, H.; Witzens, J.; Buca, D. Optically Pumped GeSn Microdisk Lasers on Si. *ACS Photon.* **2016**, *3*, 1279−1285.

(21) Park, H.-G.; Kim, S.-H.; Kwon, S.-H.; Ju, Y.-G.; Yang, J.-K.; Baek, J.-H.; Kim, S.-B.; Lee, Y.-H. Electrically Driven Single-Cell Photonic Crystal Laser. *Science* **2004**, *305*, 1444−1447.

(22) Marzban, B.; Seidel, L.; Kiyek, V.; Liu, T.; Zöllner, M.; Ikonic, Z.; Capellini, G.; Buca, D.; Schulze, J.; Oehme, M.; Witzens, J. Modeling and design of an electrically pumped SiGeSn microring laser. *Proc. SPIE* **2022**, *12006*, 120060K.

(23) Assali, S.; Elsayed, M.; Nicolas, J.; Liedke, M. O.; Wagner, A.; Butterling, M.; Krause-Rehberg, R.; Moutanabbir, O. Vacancy complexes in nonequilibrium germanium-tin semiconductors. *Appl. Phys. Lett.* **2019**, *114*, 251907.

(24) Fischer, I. A.; Wendav, T.; Augel, L.; Jitpakdeebodin, S.; Oliveira, F.; Benedetti, A.; Stefanov, S.; Chiussi, S.; Capellini, G.; Busch, K.; Schulze, J. Growth and characterization of SiGeSn quantum well photodiodes. *Opt. Exp.* **2015**, *23* (19), 25048−25057.

(25) Wirths, S.; Geiger, R.; Schulte-Braucks, C.; von den Driesch, N.; Stange, D.; Zabel, T.; Ikonic, Z.; Hartmann, J.-M.; Mantl, S.; Sigg, H.; Grützmacher, D.; Buca, D. Direct Bandgap GeSn Microdisk Lasers at 2.5 μm for Monolithic Integration on Si-Platform. *Proc. 2015 IEEE Electron Dev. Meet. (IEDM)*, Washington DC, Dec 7−9, 2015; IEEE: Piscataway, NJ, 2015; pp 36−39, https://ieeexplore.ieee.org/document/7409615 (accessed Nov 17, 2022).

(26) Borselli, M.; Johnson, T. J.; Painter, O. Beyond the Rayleigh scattering limit in high-Q silicon microdisks: Theory and experiment. *Opt. Exp.* **2005**, *13* (5), 1515−1530.

(27) Zhukov, A. E.; Moiseev, E. I.; Nadtochiy, A. M.; Fominykh, N. A.; Ivanov, K. A.; Makhov, I. S.; Dragunova, A. S.; Kryzhanovskaya, N. V.; Zubov, F. I.; Maximov, M. V.; Mintairov, S. A.; Kalyuzhnyy, N. A.; Shernyakov, Y. M.; Gordeev, N. Y. Optical loss and noise modelling in microdisk lasers with InGaAs quantum well-dots. *Proc. 2022 Int. Conf. Las. Opt. (ICLO)*, Saint Petersburg, Russian Federation, Jun 20−24, 2022, IEEE: Piscataway, NJ, 2022; https://ieeexplore.ieee.org/document/9839952 (accessed Nov 17, 2022).

(28) Marzban, B.; Stange, D.; Rainko, D.; Ikonic, Z.; Buca, D.; Witzens, J. Modeling of a SiGeSn quantum well laser. *Photon Res.* **2021**, *9*, 1234−1254.

(29) Marzban, B.; Nojic, J.; Stange, D.; Buca, D.; Witzens, J. Design of a waveguide-coupled GeSn disk laser. *Proc. 2020 IEEE Photon. Soc. Sum. Top. Meet. (SUM)*, Cabo San Lucas, Mexico, July 13−15, 2020; IEEE: Piscataway, NJ, 2020; https://ieeexplore.ieee.org/document/9161034 (accessed Nov 17, 2022).

(30) Goi, A. R.; Syassen, K.; Cardona, M. Effect of pressure on the refractive index of Ge and GaAs. *Phys. Rev. B* **1990**, *41*, 10104−10110.

(31) Cai, J.; Ishikawa, Y.; Wada, K. Strain induced bandgap and refractive index variation of silicon. *Opt. Exp.* **2013**, *21* (6), 7162−7170.

(32) Zhukov, A. E.; Moiseev, E. I.; Kryzhanovskaya, N. V.; Blokhin, S. A.; Kulagina, M. M.; Guseva, Y. A.; Mintairov, S. A.; Kalyuzhnyy, N. A.; Mozharov, A. M.; Zubov, F. I.; Maximov, M. V. Evaluation of the Impact of Surface Recombination in Microdisk Lasers by Means of High-Frequency Modulation. *Phys. Semicon. Dev* **2019**, *53* (8), 1099−1103.

(33) Burt, D.; Joo, H.-J.; Jung, Y.; Kim, Y.; Chen, M.; Huang, Y.-C.; Nam, D. Strain relaxed GeSn-on-insulator (GeSnOI) microdisks. *Opt. Exp.* **2021**, *29* (18), 28959−28967.

⊞ Recommended by ACS